CHALMERS
UNIVERSITY OF TECHNOLOGY

Control-Oriented 2D Thermal Modelling of Cylindrical Battery Cells for Optimal Tab and Surface Cooling

Citation for the original published paper (version of record):
Peprah, G., Wik, T., Huang, Y. et al (2024). Control-Oriented 2D Thermal Modelling of Cylindrical Battery Cells for Optimal Tab and Surface
Cooling. Proceedings of the American Control Conference: 4651-4656.
http://dx.doi.org/10.23919/ACC60939.2024.10644585

Control-Oriented 2D Thermal Modelling of Cylindrical Battery Cells for Optimal Tab and Surface Cooling

Godwin K. Peprah, Torsten Wik, Yicun Huang, Faisal Altaf, Changfu Zou

***Abstract*— Minimising cell thermal gradients and the average temperature rise requires an optimal combination of tab and surface cooling methods to leverage their unique advantages. This work presents a computationally efficient two dimensional (2D) thermal model for cylindrical lithium-ion battery cells that is developed based on the Chebyshev Spectral-Galerkin method and allows the independent control of tab and surface cooling channels for effective thermal performance optimisation. This obtained model is validated against a high-fidelity finite element model under the worldwide harmonised light vehicle test procedure (WLTP). Results show that the reduced-order model with as few as two states can predict the spatially resolved temperature distribution throughout the cell and that in aggressive cooling scenarios, a model order of nine states can improve accuracy by about 84%. It is also shown that even though cooling all sides of the cylindrical cell achieves the lowest average temperature rise, cooling only the top and bottom sides provides minimum radial thermal gradients.**

I. Introduction

Although the transportation sector has seen significant efforts in gradually downsizing and transitioning from the use of internal combustion engines to fully electric vehicles (EVs), it is confronted with challenges, such as a limited battery range, high costs, and thermal safety issues [1]. To ensure efficient energy utilisation, a long lifetime, and curb thermal safety phenomena, the battery needs a sophisticated thermal management system [2] that controls the battery temperature to desired values irrespective of operating profiles and the ambient environment.

Battery cells can be thermally controlled at the electrical connection tabs (terminals), cell surfaces, or both [3]. The effects of tab and surface cooling on battery thermal performance have previously been investigated in the literature. Li *et al.*, and Bolsinger showed in [4,5] that tab cooling could reduce the internal temperature inhomogeneities by about 25%, but surface cooling can maintain the lithium (Li)-ion cylindrical cell at a lower average temperature under high current rates than tab cooling. Surface and tab cooling each possess distinct advantages and drawbacks. However, to the best of our knowledge, there is currently no battery control framework in the state-of-the-art literature that systematically explores the optimal combination of these two cooling methods.

While lumped parameter thermal equivalent circuits (TECs) have been extensively used for control-oriented modelling of batteries [6,7], they can only predict average and surface temperatures and their applicability is limited to cells with small Biot numbers. Physics-based models [8] result in partial differential equations (PDEs) that govern the underlying heat diffusion. They can predict spatially distributed temperatures throughout the cell but are typically implemented via computationally expensive numerical methods, such as finite element methods (FEM), rendering them impractical for control purposes.

A computationally feasible spectral method based on the Galerkin approach was adopted to develop a low-order 2-dimensional (2D) thermal model for cylindrical cells in [9]. However, this model does not allow independent and targeted cooling control of battery tabs and surfaces, preventing its use for optimally combining tab and surface cooling for battery thermal management.

To bridge the identified research gap, we develop a new 2D battery thermal model that stems from a reformulation of the model in [9]. Unlike [9], which used a lumped lifting function that captured all sides of the cell in one go, our model decomposes the lifting function into constituent side components, enabling us to obtain independent controls for each side of the battery. In addition, we investigate different cooling scenarios and their effects on the thermal performance of cylindrical battery cells.

The developed model can accurately predict the spatially resolved temperature field throughout a cylindrical battery at a similar computational cost as TECs. Hence, the model can be useful for real-time optimal control of the cooling effort applied on battery tabs and surfaces.

II. Overview

The cell geometry of the proposed battery thermal model is shown in Fig. 1. The tabs placed on the top and bottom sides of the cylindrical cell can have different sizes. Existing designs make the tab's area much smaller than the cell's top/bottom area. Studies in [4] have demonstrated that these designs are not efficient for battery cooling merely from the tabs. Consequently, our model considers the entire area of the top/bottom as the tabs (all-tab/tabless cell design), as illustrated in Fig. 1. In the following sections, we present the

This work was funded in part by the Swedish Electromobility Centre and the Swedish Energy Agency under grant No. 13011 and in part by the Swedish Research Council under grant No. 2019-04873.

G. K. Peprah, T. Wik, Y. Huang, and C. Zou are with the Department of Electrical Engineering, Chalmers University of Technology, 41296 Gothenburg, Sweden. (Emails: godwinp@chalmers.se; tw@chalmers.se; yicun@chalmers.se; changfu.zou@chalmers.se).

F. Altaf is with the Department of Electromobility, Volvo Group Trucks Technology, 40508 Gothenburg, Sweden. (Email: faisal.altaf@volvo.com).

governing heat PDE for the cell and its associated boundary conditions. We proceed to employ the Chebyshev spectral method, and finally present the reformulation of the model, using a boundary-lifting algorithm [10].

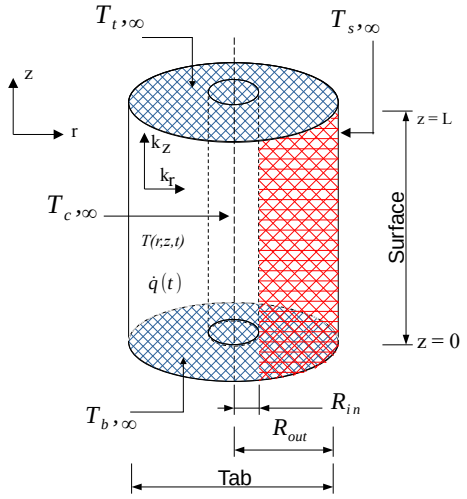

Fig. 1: Schematics of a cylindrical cell for the 2D thermal model. The blue and red-shaded areas represent the tab and surface cooling channels, respectively.

A. PDE-based Battery Thermal Model

The cylindrical cell's multi-layer structure is considered a homogeneous solid with anisotropic radial and axial thermal conductivities. Convective heat transfer is presumed to occur on the external surfaces, where the heat transfer coefficient and fluid free-stream temperatures, may differ for each surface. Heat generation is assumed to be time-varying but uniformly distributed in space, and is considered an input disturbance in our model. The governing heat equation for the cylindrical cell and its non-homogeneous convection boundary conditions are given by

$$\rho C_p \frac{\partial T}{\partial t} - k_r \frac{\partial^2 T}{\partial r^2} - \frac{k_r \partial T}{r \partial r} - k_z \frac{\partial^2 T}{\partial z^2} = q(t), \tag{1}$$

$$k_r \frac{\partial T}{\partial r} = h_s \left(T - T_{s,\infty}\right), \quad \text{at } r = R_{\text{out}} \tag{2a}$$

$$k_r \frac{\partial T}{\partial r} = -h_c \left(T - T_{c,\infty}\right), \text{ at } r = R_{\text{in}} \tag{2b}$$

$$k_z \frac{\partial T}{\partial z} = h_t \left(T - T_{t,\infty}\right), \quad \text{at } z = L \tag{2c}$$

$$k_z \frac{\partial T}{\partial z} = -h_b \left(T - T_{b,\infty}\right), \text{ at } z = 0 \tag{2d}$$

where the coefficients ρ and C_p are the volume-averaged density and specific heat capacity, respectively. $T(r,z,t)$ is the temperature distribution, t is time, $r \in [R_{\text{in}}, R_{\text{out}}]$ and $z \in [0, L]$ are the position coordinates in the r and z-directions, with R_{in} and R_{out} being the inner and outer radii, respectively, and L being the length of the battery. k_r and k_z are the anisotropic thermal conductivities in the r and z directions, and $q(t)$ is the volumetric heat generation rate. The fluid free-stream temperatures are given by $\{T_\varphi; \varphi = s, c, t, b\}$ for the curved surface, core, top and bottom sides of the battery, respectively. The corresponding convection coefficients are given by $\{h_\varphi; \varphi = s, c, t, b\}$. We note that negligible cooling occurs in the core area of the cylindrical cell and thus, $h_c = 0$ in (2b).

We transform the scale from the physical, i.e., $r \in [R_{\text{in}}, R_{\text{out}}]$, $z \in [0, L]$ to $\{\tilde{r}, \tilde{z}\} \in [-1, 1]$, to simplify the use of the orthogonal polynomial basis functions, such as the Chebyshev polynomials [11]. The scaled governing equation is then given by

$$\rho C_p \frac{\partial T}{\partial t} - \alpha^2 k_r \frac{\partial^2 T}{\partial \tilde{r}^2} - \gamma \frac{\partial T}{\partial \tilde{r}} - \beta^2 k_z \frac{\partial^2 T}{\partial \tilde{z}^2} = q, \tag{3}$$

with the scaling factors $\alpha = \frac{2}{R_{\text{out}} - R_{\text{in}}}$, $\gamma = \frac{\alpha^2 k_r}{1 + \alpha R_{\text{in}} + \tilde{r}}$, $\beta = \frac{2}{L}$, and subject to the boundary conditions

$$\begin{pmatrix} h_s \\ -h_c \end{pmatrix} T + b_\pm \frac{\partial T}{\partial \tilde{r}} = \begin{pmatrix} u_s \\ u_c \end{pmatrix} \text{ at } \tilde{r} = \pm 1, \tag{4a}$$

$$\begin{pmatrix} h_t \\ -h_b \end{pmatrix} T + d_\pm \frac{\partial T}{\partial \tilde{z}} = \begin{pmatrix} u_t \\ u_b \end{pmatrix} \text{ at } \tilde{z} = \pm 1, \tag{4b}$$

where $b_\pm = -\alpha k_r$, $d_\pm = -\beta k_z$, $u_s = h_s T_{s,\infty}$, $u_c = -h_c T_{c,\infty}$, $u_t = h_t T_{t,\infty}$, and $u_b = -h_b T_{b,\infty}$.

B. Solution to Governing Heat Equation

The solution to the heat equation, (3) is composed of two parts as follows

$$T(\tilde{r}, \tilde{z}, t) = T_h(\tilde{r}, \tilde{z}, t) + T_p(\tilde{r}, \tilde{z}, t), \tag{5}$$

where T_h is the unknown homogeneous solution that satisfies the modified problem for the cylindrical cell as

$$\begin{aligned} &\rho C_p \frac{\partial T_h}{\partial t} - \alpha^2 k_r \frac{\partial^2 T_h}{\partial \tilde{r}^2} - \gamma \frac{\partial T_h}{\partial \tilde{r}} - \beta^2 k_z \frac{\partial^2 T_h}{\partial \tilde{z}^2} \\ &= q - \left(- \alpha^2 k_r \frac{\partial^2 T_p}{\partial \tilde{r}^2} - \gamma \frac{\partial T_p}{\partial \tilde{r}} - \beta^2 k_z \frac{\partial^2 T_p}{\partial \tilde{z}^2} \right) \triangleq q^*, \end{aligned} \tag{6}$$

and has homogeneous boundary conditions

$$\begin{pmatrix} h_s \\ -h_c \end{pmatrix} T_h(\pm 1, \tilde{z}) + b_\pm \frac{\partial T_h}{\partial \tilde{r}}(\pm 1, \tilde{z}) = 0, \tag{7a}$$

$$\begin{pmatrix} h_t \\ -h_b \end{pmatrix} T_h(\tilde{r}, \pm 1) + d_\pm \frac{\partial T_h}{\partial \tilde{z}}(\tilde{r}, \pm 1) = 0. \tag{7b}$$

T_p is the particular solution that satisfies the original boundary conditions (4). T_p is determined by a boundary lifting function, which will be discussed in Section III-A. The solution (5) is approximated by a finite sum T_N, as

$$T \approx T_N = T_{h,N} + T_{p,N} = \sum_{m=0}^{M} \sum_{n=0}^{N} c_{mn}(t) \phi_m^{\tilde{r}} \phi_n^{\tilde{z}} + T_{p,N}, \tag{8}$$

where $T_{h,N}$ and $T_{p,N}$ are the approximated solutions of T_h and T_p, respectively, by a finite sum of functions. M and N are the number of Chebyshev basis functions in

each dimension, and $\phi_m^{\tilde{r}}$ and $\phi_n^{\tilde{z}}$ are the corresponding basis functions, which must satisfy the homogeneous boundary conditions (7a) and (7b), respectively. $c_{mn}(t)$ are the unknown solution coefficients. Details of the basis functions can be found in [9,11]. Using the notation $\Big(f,\eta\Big) = \int_{-1}^{1}\int_{-1}^{1} f(\tilde{r},\tilde{z})\eta(\tilde{r},\tilde{z})d\tilde{r}d\tilde{z}$, which represents the inner product weighted by a test function η in the domain $\tilde{r},\tilde{z}$, the standard Galerkin approximation of the modified problem (6) is given by

$$\begin{aligned}\Bigg(r\Big[\rho C_p\frac{\partial T_{h,N}}{\partial t} - \alpha^2 k_r\frac{\partial^2 T_{h,N}}{\partial \tilde{r}^2} - \gamma\frac{\partial T_{h,N}}{\partial \tilde{r}} \\ -\beta^2 k_z\frac{\partial^2 T_{h,N}}{\partial \tilde{z}^2}\Big],\eta\Bigg) = \Big(rq^*,\eta\Big),\end{aligned} \tag{9}$$

where $r = \frac{1+\tilde{r}+\alpha R_{\text{in}}}{\alpha}$ included on each side accounts for the cylindrical coordinates. Next, we discuss the form of the expansion of $T_{p,N}$ in terms of the basis functions.

III. Model Reformulation

Unlike [9,10], which used a lumped boundary lifting function that merged all the sides of the cell into a single function, we show below our approach, which decomposes the lifting function into its constituent side components. This approach makes it possible to obtain independent control signals for each side (tab and surface) of the cell. The complete state space thermal model is derived afterwards.

A. Particular solution, $T_p(\tilde{r},\tilde{z},t)$

We derive the boundary lifting function T_p, that satisfies the non-homogeneous boundary conditions (4). The boundary conditions are fulfilled in a weak sense, i.e., as additional basis functions are incorporated, the solution gradually approaches convergence, resulting in $T_p \approx T_{p,N}$.

In this study, we propose that $T_{p,N}$ is composed of the constituent cell side components and can be expressed as

$$T_{p,N}(\tilde{r},\tilde{z},t) = T^s_{p,N} + T^t_{p,N} + T^b_{p,N}, \tag{10}$$

where we assume the surface, top, and bottom side components are given by the expansions

$$T^s_{p,N} = \sum_{n=0}^{N}\Big(d_n^{s,1}\tilde{r} + d_n^{s,2}\tilde{r}^2\Big)\phi_n^{\tilde{z}}, \tag{11a}$$

$$T^{\{t,b\}}_{p,N} = \sum_{m=0}^{M}\Big(d_m^{\{t,b\},1}\tilde{z} + d_m^{\{t,b\},2}\tilde{z}^2\Big)\phi_m^{\tilde{r}}, \tag{11b}$$

with $\big\{d^{\varphi,\{1,2\}}_{\{m,n\}};\varphi = s,t,b;\{m,n\} = 0,\cdots,N\big\}$ being the coefficients to be determined. The core's component $T^c_{p,N} = 0$. We define the conditions at the vertical and horizontal sides below. For the curved surface, we have

$$h_s T^s_{p,N} + b_+\frac{\partial T^s_{p,N}}{\partial \tilde{r}} \approx u_s \;\; at \;\; \tilde{r} = 1, \tag{12}$$

where $\approx$ denotes weakly satisfying conditions. Substituting (11a) into (12) and with $\tilde{r} = 1$, gives

$$\sum_{n=0}^{N}\Big[d_n^{s,1}(h_s + b_+) + d_n^{s,2}(h_s + 2b_+)\Big]\phi_n^{\tilde{z}} \approx u_s. \tag{13}$$

Replacing (13) with the weighted integral equation, $\Big\langle f,\eta\Big\rangle_{\tilde{z}} = \int_{-1}^{1} f(\tilde{z})\eta(\tilde{z})d\tilde{z}$, gives

$$\sum_{n=0}^{N}\Big[d_n^{s,1}(h_s+b_+)+d_n^{s,2}(h_s+2b_+)\Big]\Big\langle\phi_n^{\tilde{z}},\phi_i^{\tilde{z}}\Big\rangle_{\tilde{z}} = \Big\langle u_s,\phi_i^{\tilde{z}}\Big\rangle_{\tilde{z}}, \tag{14}$$

for $i = 0,\cdots,N$. Adopting a similar process for the top, and bottom sides we have

$$\begin{aligned}\sum_{m=0}^{M}\Big[d_m^{\{t,b\},1}\Big(h^{\{t,b\}} + d_\pm\Big) + d_m^{\{t,b\},2}\Big(\pm h^{\{t,b\}} \pm 2d_\pm\Big)\Big] \\ \cdot\Big\langle\phi_m^{\tilde{r}},\phi_i^{\tilde{r}}\Big\rangle_{\tilde{r}} = \Big\langle u_{\{t,b\}},\phi_i^{\tilde{r}}\Big\rangle_{\tilde{r}},\end{aligned} \tag{15}$$

for $i = 0,\cdots,M$, and $\Big\langle f,\eta\Big\rangle_{\tilde{r}} = \int_{-1}^{1} rf(\tilde{r})\eta(\tilde{r})d\tilde{r}$. Defining matrices for the surface, top, and bottom sides, as

$$V^s = \int_{-1}^{1}\phi_n^{\tilde{z}}\phi_i^{\tilde{z}}d\tilde{z}, \quad \text{and} \quad H^{\{t,b\}} = \int_{-1}^{1} r\phi_m^{\tilde{r}}\phi_i^{\tilde{r}}d\tilde{r}, \tag{16}$$

and their corresponding source terms

$$S^s = u_s\int_{-1}^{1}\phi_i^{\tilde{z}}d\tilde{z}, \quad \text{and} \quad S^{\{t,b\}} = u_{\{t,b\}}\int_{-1}^{1} r\phi_i^{\tilde{r}}d\tilde{r}, \tag{17}$$

(14)-(15) are equivalent to the following linear systems

$$\begin{aligned}V^s\Big[d_n^{s,1}(h_s + b_+) + d_n^{s,2}(h_s + 2b_+)\Big] = S^s \\ H^t\Big[d_m^{\{t,b\},1}\big(h^{\{t,b\}} + d_\pm\big) + d_m^{\{t,b\},2}\big(\pm h^{\{t,b\}} \pm 2d_\pm\big)\Big] \\ = S^{\{t,b\}},\end{aligned} \tag{18}$$

which can be solved for the corresponding $\Big\{d^{\varphi,\{1,2\}}_{\{m,n\}};\varphi = s,t,b\Big\}$ vectors of unknown expansion coefficients given by

$$\begin{aligned}d^{s,1} &= V_4 S^s(V^s)^{-1}, \qquad d^{s,2} = -V_1\Big(\frac{v_3}{v_1}\Big)S^s(V^s)^{-1} \\ d^{t,1} &= H_4 S^t(H^t)^{-1}, \qquad d^{t,2} = -H_1\Big(\frac{h_3}{h_1}\Big)S^t(H^t)^{-1} \\ d^{b,1} &= -H_4\Big(\frac{h_2}{h_4}\Big)S^b(H^b)^{-1}, \quad d^{b,2} = H_1 S^b(H^b)^{-1}\end{aligned} \tag{19}$$

where $V_{\{1,4\}} = \frac{v_{\{1,4\}}}{v_1 v_4 - v_2 v_3}$, $H_{\{1,4\}} = \frac{h_{\{1,4\}}}{h_1 h_4 - h_2 h_3}$, $\{v_1,v_2,v_3,v_4\} = \{h_s + b_+, h_s + 2b_+, h_c + b_-, -h_c - 2b_-\}$, and $\{h_1,h_2,h_3,h_4\} = \{h_t + d_+, h_t + 2d_+, -h_b + d_-, -h_b - 2d_-\}$.

B. State space equation

Denoting the basis functions for the approximate solution for T_h by $\xi_i = \phi_m^{\tilde{r}}\phi_n^{\tilde{z}}$ and that from the test function by $\eta_j = \phi_m^{\tilde{r}}\phi_n^{\tilde{z}}$, for $i,j = 0,\cdots,N$; (9) is equivalent to the state space equation

$$G\dot{x} = Ax + Bu + Fw, \tag{20}$$

where

$$x = [(c_{00}, c_{10}, \cdots, c_{N0}), \cdots, (c_{0N}, c_{1N}, \cdots, c_{NN})]^T \quad (21)$$

$$u = \begin{bmatrix} u_s & u_t & u_b \end{bmatrix}^T, \quad w = q, \quad (22)$$

are the states, control inputs, and the disturbance, respectively. The system matrices are defined below. The element in the i-th row and j-th column of matrix G, and vector F are given by

$$G(i,j) = \rho C_p\big(r\xi_i, \eta_j\big), \quad F(i,1) = \big(r, \eta_j\big). \quad (23)$$

Similarly, $A(i,j)$ is given by

$$\left(r\left[\alpha^2 k_r \frac{\partial^2 \xi_i}{\partial \tilde{r}^2} + \gamma \frac{\partial \xi_i}{\partial \tilde{r}} + \beta^2 k_z \frac{\partial^2 \xi_i}{\partial \tilde{z}^2}\right], \eta_j\right) \quad (24)$$

and $B(i, \{1,2,3\})$ are given by

$$\left(r\left[\alpha^2 k_r \frac{\partial^2 T_{p,N}^{\{s,t,b\}}}{\partial \tilde{r}^2} + \gamma \frac{\partial T_{p,N}^{\{s,t,b\}}}{\partial \tilde{r}} + \beta^2 k_z \frac{\partial^2 T_{p,N}^{\{s,t,b\}}}{\partial \tilde{z}^2}\right], \eta_j\right) \quad (25)$$

Fig. 2 shows temperature locations in the cylindrical cell. For brevity, we choose the outputs of the system as the temperatures at the mid-surface $T_{s,m}$, mid-core $T_{c,m}$, mid-top $T_{t,m}$, and mid-bottom $T_{b,m}$. The output equation is then

$$y = Cx + T_{p,N}, \quad (26)$$

where

$$y = \begin{bmatrix} T_{s,m} & T_{c,m} & T_{t,m} & T_{b,m} \end{bmatrix}^T, \quad (27a)$$

$$T_{p,N} = \begin{bmatrix} T_{p,N}^s & T_{p,N}^c & T_{p,N}^t & T_{p,N}^b \end{bmatrix}^T, \quad (27b)$$

$$C(1,i) = \xi_i(\tilde{r} = 1, \tilde{z} = 0), \quad (28a)$$

$$C(2,i) = \xi_i(\tilde{r} = -1, \tilde{z} = 0), \quad (28b)$$

$$C(3,i) = \xi_i(\tilde{r} = 0, \tilde{z} = 1), \quad (28c)$$

$$C(4,i) = \xi_i(\tilde{r} = 0, \tilde{z} = -1). \quad (28d)$$

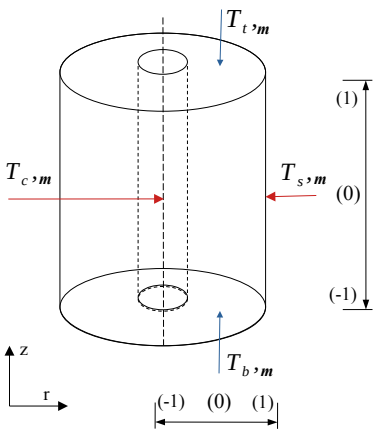

Fig. 2: Temperature locations in cylindrical cell.

IV. Results and Discussion

A. Simulation Setup

A large format lithium-iron-phosphate cylindrical cell is chosen for the simulation and validation. Its parameters include dimension-related parameters, i.e. L = 198 mm, R_{in} = 4 mm and R_{out} = 32 mm [12], and thermodynamic parameters, β = 1684 kJ/(m^{3}K), k_r = 0,67 W/(mK) and k_z = 66,6 W/(mK) [13]. The thermal model is validated against an FEM model with an extremely fine mesh of 3610 triangular elements implemented in COMSOL Multiphysics v6.0. The validation is conducted under the heat generation profile of the worldwide harmonised light vehicle test procedure (WLTP) [14], representative of a wider range of driving conditions in urban, suburban, and highway roads. The volumetric heat generation rate q, is assumed to be given by the simplified heat generation model

$$q = I(V - V_{ocv})/V_b, \quad (29)$$

where I, V, V_{ocv}, and V_b are the load current, terminal voltage, open-circuit voltage, and cell volume, respectively. (29) includes the ohmic heating and energy dissipated in the electrode over-potentials. For more accurate modelling of q, reversible heat, such as entropic heat can be included [7].

We simulate three different cooling scenarios, labelled CS_1-CS_3, based on where the cooling action is imposed. They involve cooling of the surface, and/or tab areas, and are summarised in Table I. We also note that CS_3 is representative of immersion cooling [15]. In all cases, we set all temperatures to 15 °C. Forced convection liquid cooling (for instance, using a cooling plate) via water or glycol which typically has a large convection coefficient h, of about 400 Wm^{-2}K^{-1} [16], is assumed to apply in areas where tab or surface cooling occurs. Mild air convection with a small $h \approx 30$ Wm^{-2}K^{-1} occurs in areas not exposed to active cooling.

TABLE I: Cooling scenarios, CS_1-CS_3, investigated.

Cooling Scenarios	**Label**
Surface cooling only	CS_1
Tab cooling only (bottom + top sides)	CS_2
Tab (bottom + top sides) + Surface cooling	CS_3

B. Model Validation

The results of the three cooling scenarios, CS_1-CS_3, are reported in Fig. 3. The absolute errors between model orders N = 2, 4, 9 and 25, relative to the benchmark FEM are shown below each scenario.

In CS_1 (Fig. 3a), the max and mean absolute errors with N = 2, are 0,22 °C and 0,10 °C, respectively, and with N = 25, are 0,14 °C and 0,03 °C, respectively. Using the mean error, N = 25 produces about 0,07 °C improvement in accuracy as compared to N = 2, thus a marginal increase in accuracy. It can be concluded that a model order of N = 2 states, captures the thermal dynamics sufficiently well in CS_1. In CS_2 and

CS_3, which have aggressive cooling because multiple sides are cooled, it was observed that at least a model order of $N = 4$ was necessary to accurately capture the thermal dynamics. For CS_2 (Fig. 3b), N = 4 gives max absolute error of $0{,}11\,^{\circ}\mathrm{C}$ and a mean of $0{,}10\,^{\circ}\mathrm{C}$, whilst N = 25 gives no error. N = 9 gives $0{,}02\,^{\circ}\mathrm{C}$ and $0{,}01\,^{\circ}\mathrm{C}$, which represents about $0{,}08\,^{\circ}\mathrm{C}$ improvement in accuracy compared to N = 4. In this case, a model order of N = 4 is satisfactory. Finally, in CS_3 (Fig. 3c), where model orders of N = 9 and 25 were chosen to give better resolution of the thermal dynamics, $N = 25$ gives a marginal $0{,}12\,^{\circ}\mathrm{C}$ improvement in accuracy compared to N = 9, showing that N = 9 is sufficient.

To summarise, the thermal dynamics can be faithfully captured with as few as N = 2 states in mild cooling scenarios. However, using N = 9 in these mild scenarios only gives a marginal accuracy improvement of about $0{,}072\,^{\circ}\mathrm{C}$. With aggressive cooling (cooling multiple sides), N = 2 is not sufficient but increasing the order to N = 9 substantially enhances accuracy, achieving an improvement of about 84%.

C. Thermal Performance Discussion

We observe that in all scenarios, the cell experiences higher radial thermal gradients $T_{\mathrm{g,r}}$, than axial thermal gradients $T_{\mathrm{g,z}}$. This is due to the lower thermal conductivity in the r-direction. Thus, $T_{\mathrm{g,r}}$ is used as a performance metric instead of $T_{\mathrm{g,z}}$ in this work. The average temperature, $\bar{T}$ = $15{,}81\,^{\circ}\mathrm{C}$ in CS_1 is the highest in all cases because it has only one side exposed to cooling. More areas exposed to cooling, as in CS_3, result in higher heat removal and thus the lowest average temperature ($\bar{T}$ = $15{,}31\,^{\circ}\mathrm{C}$). However, CS_3 does not produce the lowest $T_{\mathrm{g,r}}$. CS_2 provides the lowest ($T_{\mathrm{g,r}}$ = $1{,}25\,^{\circ}\mathrm{C/m}$) amongst all three cases, followed by CS_3 with $T_{\mathrm{g,r}}$ = $3{,}03\,^{\circ}\mathrm{C/m}$. The lowest $T_{\mathrm{g,r}}$ in CS_2 can be attributed to symmetric cooling on both the top and bottom sides of the cell and twice as much area for tab cooling. In addition, all electrodes get access to cooling at the same time in CS_2 because of the rolled electrode layer structure. On the contrary, in the surface cooling scenario (CS_1), the outer layers get cooled first, before the internal layers, leading to inhomogeneous cooling and consequently the highest ($T_{\mathrm{g,r}}$ = $4{,}53\,^{\circ}\mathrm{C/m}$). CS_2 also provides the lowest temperature difference, ($\Delta T = T_{\max} - T_{\min}$ = $4{,}23\,^{\circ}\mathrm{C}$), amongst all cooling cases. Table II summarises the results of the three cooling scenarios.

In summary, CS_2 provides the most homogeneous cooling effect and should result in more homogeneous ageing, leading to an extended lifetime. It, however, does that at the expense of a higher $\bar{T}$ in the cell. Including surface cooling, as in CS_3, will decrease $\bar{T}$ but will in turn increase $T_{\mathrm{g,r}}$. These two conflicting thermal performance objectives motivate an optimal scheme selection, which the developed model (20) and (26), will be pivotal in achieving. Our control-oriented model will also be useful in providing targeted control to any side of the cell. We note that CS_3 gives the smallest temperature rise, ($T_{\max}$=$18{,}79\,^{\circ}\mathrm{C}$), which means, the chances of getting closer to the onset temperature of thermal runaway will be reduced under cooling scenario CS_3. We also observe that in all cases, surface temperatures are the lowest, and temperatures in the core exhibited the highest values, as expected. After heat is generated from different electro-chemical processes in the battery, the heat is conducted mostly radially, via the solid material to the battery surface and then dissipated to the cooling medium. In the cylindrical cell, the radial thermal conductivity is two orders of magnitude lower than that of the axial direction, which presents a significant bottleneck in heat transfer to the surface. This, aside from the absence of cooling in the core, also accounts for why the core temperature has the highest value. Factors such as an increased cooling flow rate and the use of battery materials with a higher thermal conductivity can increase the cooling efficiency and facilitate the lowering of the core temperature. This suggests the need to develop a control scheme that targets several relevant objectives and constrains the core temperature to a safe limit. In addition, the proposed model can be vital in monitoring and estimating the core temperature, which is typically not measured by sensors, helping to mitigate irreversible ageing and even thermal runaway, in a timely fashion.

The computational complexity of the proposed thermal model is mainly dependent on the number of basis functions N, and temperature outputs of the model. In this work, the model is run under the WLTP on a MacBook Pro with a 2,6GHz 6-Core Intel Core i7 processor and 16GB RAM. Selecting the outputs in (27a), the elapsed time of the model was on average about 0,11s and 0,59s for two and nine states respectively, which is comparable to the TECs in [17]. This is a good indication that the model can be used for real-time optimal control and can be scaled to a module and pack level with moderate computational efficiency.

TABLE II: Thermal performance merits of three scenarios.

Scenarios	T	**Max** $T_{\mathbf{g,r}}$	**Max** $T_{\mathbf{g,z}}$	$T_{\max}$	ΔT
CS_1	15,81	4,53	0,14	20,14	5,20
CS_2	15,73	1,25	0,69	19,11	4,23
CS_3	15,31	3,03	1,55	18,79	4,47

V. Conclusion

This paper has presented a 2D battery thermal model, which is based on the Chebyshev Spectral-Galerkin approach and allows independent control signals for the tab and surface cooling channels, making it suitable for online optimisation of thermal performance. The developed model can predict the spatially resolved full temperature distribution throughout the cell at a low computational cost, which is comparable to that of thermal equivalent circuits. The proposed modelling approach was evaluated through various combinations of tab and surface cooling scenarios under real-world vehicle driving profiles. It has been shown that battery thermal dynamics can be faithfully captured by a two-state reduced-order model and that in aggressive cooling scenarios, a

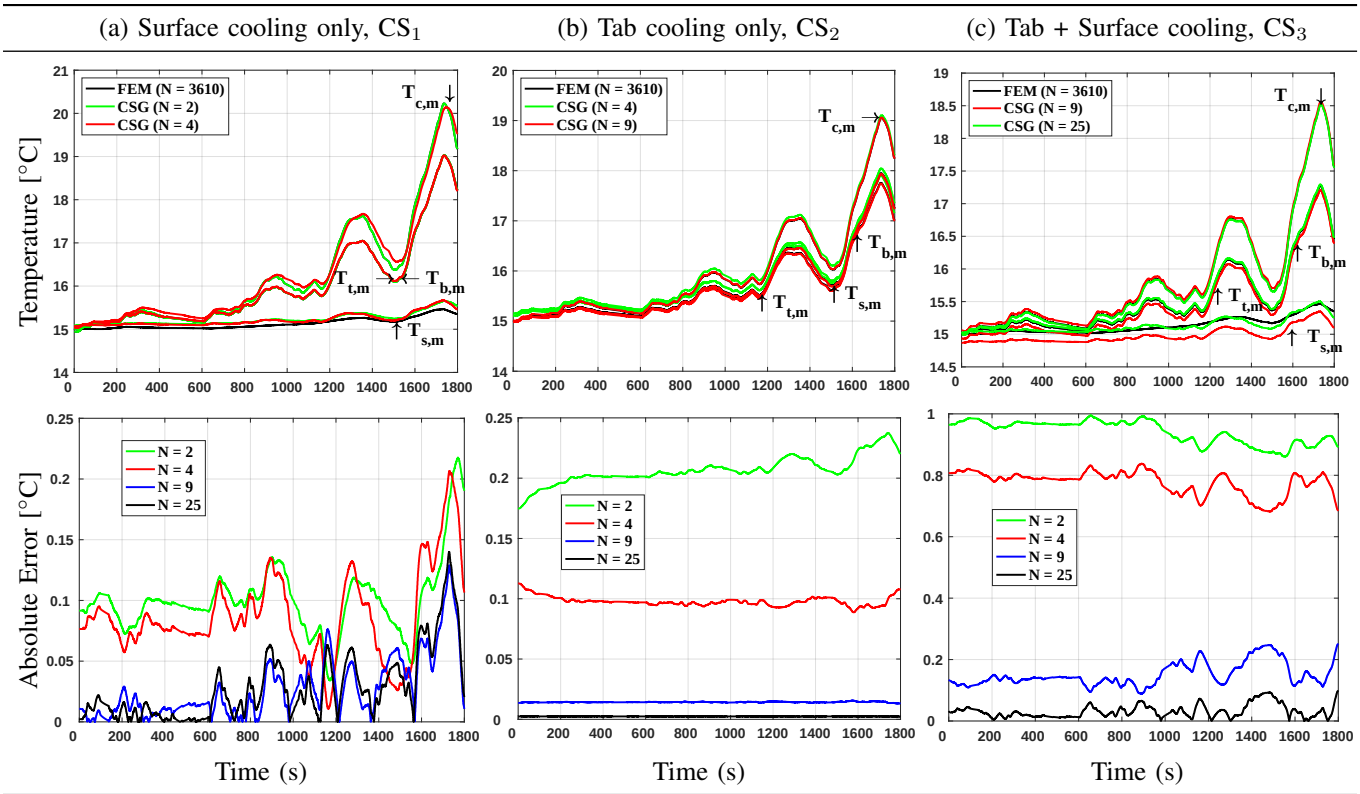

Fig. 3: Comparison of developed CSG thermal model of different orders N, against FEM with element number N = 3610, together with the absolute errors for the three cooling scenarios investigated. The models were compared at the output temperature points (27a).

model order of nine states can improve accuracy by about 84%. Results also showed that cooling all sides of the cell led to the lowest average temperature rise, while cooling the top and bottom sides only resulted in the lowest radial thermal gradient. The proposed model will be instrumental in selecting the best cooling schemes to reduced cell average temperature rise and thermal gradients.

REFERENCES

[1] M. J. Lain, J. Brandon, and E. Kendrick, "Design strategies for high power vs. high energy lithium ion cells," *Batteries*, vol. 5, no. 4, p. 64, 2019.

[2] J. Lin *et al.*, "A rev. on recent progress, challenges and perspective of battery thermal manage. system," *Int. J. Heat and Mass Transfer*, vol. 167, p. 120834, 2021.

[3] Y. Zhao *et al.*, "How to cool lithium ion batteries: optimising cell design using a thermally coupled model," *J. Electrochem. Soc.*, vol. 166, no. 13, p. A2849, 2019.

[4] S. Li *et al.*, "Optimal cell tab design and cooling strategy for cylindrical lithium-ion batteries," *J. Power Sources*, vol. 492, p. 229594, 2021.

[5] C. Bolsinger and K. P. Birke, "Effect of different cooling configurations on thermal gradients inside cylindrical battery cells," *J. Energy Storage*, vol. 21, pp. 222–230, 2019.

[6] G. Peprah *et al.*, "Optimal load sharing in reconfigurable battery systems using an improved model predictive control method," in *2021 29th Mediterranean Conf. Control and Automat. (MED)*, pp. 979–984. IEEE, 2021.

[7] X. Lin *et al.*, "A lumped-parameter electro-thermal model for cylindrical batteries," *J. Power Sources*, vol. 257, pp. 1–11, 2014.

[8] V. Srinivasan and C. Wang, "Anal. of electrochemical and thermal behavior of li-ion cells," *J. Electrochem. Soc.*, vol. 150, no. 1, p. A98, 2002.

[9] R. R. Richardson, S. Zhao, and D. A. Howey, "On-board monitoring of 2-d spatially-resolved temperature in cylindrical lithium-ion batteries: Part I. Low-order thermal modelling," *J. Power Sources*, vol. 326, pp. 377–388, 2016.

[10] E. H. Doha and A. H. Bhrawy, "An efficient direct solver for multi-dimensional elliptic robin boundary value problems using a legendre spectral-galerkin method," *Comput. & Math. with Appl.*, vol. 64, no. 4, pp. 558–571, 2012.

[11] J. Shen, T. Tang, and L.-L. Wang, *Spectral methods: algorithms, anal. and appl.* Springer Science & Business Media, 2011, vol. 41.

[12] V. Roscher *et al.*, "Synchronisation using wireless trigger-broadcast for impedance spectrosc. of battery cells," in *IEEE Sensors Appl. Symp.*, pp. 1–6. IEEE, 2015.

[13] M. Fleckenstein *et al.*, "Thermal impedance spectrosc.-a method for the thermal characterization of high power battery cells," *J. Power Sources*, vol. 223, pp. 259–267, 2013.

[14] P. Mock *et al.*, "The wltp: How a new test procedure for cars will affect fuel consumption values in the eu," *Intern. council on clean transp.*, vol. 9, no. 3547, 2014.

[15] C. Roe *et al.*, "Immersion cooling for lithium-ion batteries–a review," *J. Power Sources*, vol. 525, p. 231094, 2022.

[16] P. R. Tete, M. M. Gupta, and S. S. Joshi, "Developments in battery thermal manage. systems for electric vehicles: A technical rev." *J. of Energy Storage*, vol. 35, p. 102255, 2021.

[17] Y. Li *et al.*, "Control-oriented modeling of all-solid-state batteries using physics-based equivalent circuits," *IEEE Trans. on Transp. Electrific.*, vol. 8, no. 2, pp. 2080–2092, 2021.